Composites Communications 55 (2025) 102321

Contents lists available at ScienceDirect

Composites Communications

journal homepage: www.elsevier.com/locate/coco

3D-printing magnetic susceptor filament for induction welding of thermoplastic composite sandwich panels

R.G. Martin [a], C. Jonasson [b], C. Johansson [b], J.R. Tavares [c], M. Dubé [a,*]

[a] CREPEC, Mechanical Engineering, Ecole de Technologie Supérieure (ETS), Montréal, Canada
[b] RISE Research Institutes of Sweden, Göteborg, Sweden
[c] CREPEC, Chemical Engineering, Polytechnique Montréal, Montréal, Canada

ARTICLE INFO

Keywords:
Induction welding
3D-printing
Thermoplastic composites

ABSTRACT

A magnetic susceptor in a printable filament form is developed for the induction welding of thermoplastic composites. The susceptor is based on Ni particles embedded in a poly-ether-imide matrix. It is extruded and spooled to form a filament which can then be 3D-printed. The susceptor produces heat by hysteresis losses due to the magnetic properties of the Ni particles. As opposed to other typical electrically conductive heating elements, no percolation threshold needs to be achieved to produce heat as the Ni particles individually heat up when exposed to the induction coil's magnetic field. The heating efficiency of the susceptor filament and its deposition by the fused filament fabrication technique are demonstrated. The susceptor is used to assemble all thermoplastic composite sandwich panels. The sandwich samples are tested by the flatwise tensile test and a tensile strength of 4.6 MPa is obtained, which is equivalent to or higher than reported strengths for typical aerospace-grade sandwich panels. The printable susceptor opens the way to new induction welding or heating applications as it can be printed on a surface to produce a desired heating pattern.

1. Introduction

1.1. Induction welding

Induction welding of thermoplastic composites relies on the application of an alternating (AC) magnetic field using an induction coil to dissipate heat at the interface of the two adherends to be joined. The generation of heat is performed either through induced eddy currents in electrically-conductive materials (such as metallic meshes, carbon fibre reinforced polymers or conductive films) ([1–4]), or through magnetic hysteresis losses in ferromagnetic materials ([5–7]). In the latter, magnetic particles are dispersed inside a film of thermoplastic polymer, usually the same as the adherend's matrix. This heating element is called a magnetic susceptor, and it presents the interesting advantage of containing a discontinuous filler that does not need to reach the percolation threshold to generate heat, unlike those relying on electrical conductivity ([6,8,9]). Each particle has the intrinsic ability to dissipate heat when subjected to a time-varying magnetic field and, if properly selected, the Curie temperature of the particle material can provide an inherent safety barrier against overheating.

1.2. 3D-printing magnetic susceptor filament

In recent years, filaments for Fused Filament Fabrication (FFF) made of ferromagnetic particles dispersed in a polymeric matrix have been developed. Their applications range from microwave electronics [10] to hyperthermia treatment [11]. As reported by Ehrmann et al., the magnetic particles that are used to produce these materials vary from Si-Fe alloys to hard magnets, depending on the desired coercivity and magnetic strength [12]. Regarding the thermoplastic matrix of the filament, various studies have been published using a wide range of polymers, from poly-ethylene (PE) [13] or poly-lactic acid (PLA) ([14,15]) to acrylonitrile butadiene styrene (ABS) [16] or poly-amide 12 (PA12) ([17,18]). Magnetic composites using high-performance thermoplastic polymer like poly-ether-ether-ketone (PEEK) as the matrix have also been reported [19].

In the case of induction welding, the use of a magnetic susceptor in the form of a 3D-printing filament offers the possibility to locate the heat generation and limit the quantity of added material. Galarreta et al. demonstrated the induction heating properties of a PLA-(polycarbonate)-magnetite 3D-printed composite material [14]. However, the use of a 3D-printed material exhibiting induction heating properties as a magnetic susceptor for induction welding to join thermoplastic

* Corresponding author.
E-mail address: martine.dube@etsmtl.ca (M. Dubé).

https://doi.org/10.1016/j.coco.2025.102321
Received 10 January 2025; Received in revised form 17 February 2025; Accepted 18 February 2025
Available online 19 February 2025

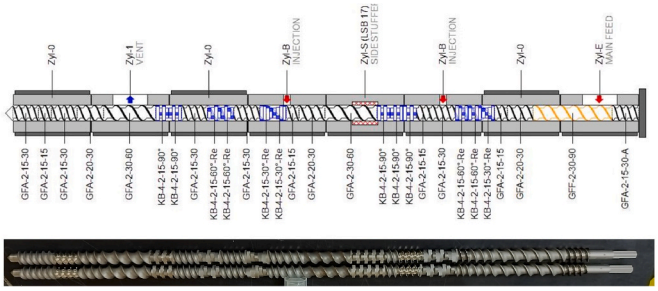

Fig. 1. Leistritz extruder screws profile, extruding material from right to left. Mixing sections are highlighted in blue and transport sections in black. The initial transport section located below the main feeding point is highlighted in yellow.

adherends has never been demonstrated. This paper aims to prove the feasibility of using this innovative type of induction welding susceptor. As pointed out by Mazeeva et al., the addition of filler particles into a polymeric matrix increases its viscosity, and the brittleness of the resulting 3D-printing filament [20]. This shows the interest of minimizing the volume content of magnetic particles in the filament. There is therefore a trade-off to find between the induction heating capabilities and the particulate content.

1.3. Sandwich structures

One well-established solution to produce light and mechanically resistant structures is to use sandwich panels. These structures are composed of two thin outer layers, known as facesheets or skins, located on top and bottom of a low-density core material. The core (polymeric foam, or aramid, aluminium or thermoplastic honeycomb core) provides compression stiffness and strength, and the facesheets (typically carbon fibre or glass fibre reinforced polymers) contribute to the tensile and bending strength. High-performance composites are typically used for the facesheets as they offer an ideal combination of light weight and good mechanical properties. While adhesive bonding is currently the preferred method to join skins to core in sandwich panels, the use of thermoplastic polymers and composites for both parts of the structure allows for the implementation of thermoplastic welding techniques for the skin/core joining [21]. The major advantages compared to oven- or autoclave-cured adhesives are the limited to absent requirements for surface preparation and the shorter cycle time. The authors of this paper have previously demonstrated that induction welding can be used to join glass fibre reinforced PEEK (GF/PEEK) skins to 3D-printed poly-ether-imide (PEI) honeycomb cores using a vacuum assisted induction welding technique [7]. This method was also successfully applied to carbon fibre-based skins, although in that case no susceptors were used as the heat generation relied on direct heating of the carbon fibres [4]. To assemble GF/PEEK sandwich panels by induction welding, PEI-based susceptor films containing nickel (Ni) particles were used, due their heating capabilities and weldability [7,22].

Here, the objective is to demonstrate the feasibility of assembling GF/PEEK skins to 3D-printed PEI honeycomb core by using a 3D-printed PEI/Ni susceptor layer, directly deposited on top of the honeycomb cell walls during the manufacturing step of the core. This minimizes the added mass of material and localizes the heat dissipation at the region of contact between the honeycomb core and skin, instead of on top of the open cells where it is not needed. To do so, a PEI/Ni 3D-printing filament is first be developed and characterized, before being printed on the core and used to weld the facesheets. The welded sandwich panels are then characterized to assess the mechanical resistance of the skin/core weld.

2. Materials and methodology

2.1. Susceptor filament manufacturing

The susceptor is constructed from Ni particles (average diameter 5 μm) from Sigma-Aldrich and PEI ULTEM 1010 (glass transition temperature = 215 °C) in powder form from SABIC. PEI powder and Ni particles are pre-mixed by hand to ensure good distribution, then the material is fed to an extruder. The Ni concentration is fixed at 10%vol.

A Leistritz ZSE18HP-400 twin-screw extruder is used to produce large quantities of PEI/Ni filament. The screws are equipped with different transport and mixing sections, as presented in detail in Fig. 1. A 1.75 mm nozzle is mounted at the extremity of the extruder. Eight heating zones are available.

- The first one (where the material is fed to the extruder) is set to 260 °C to avoid melting the material too early and clogging the feeding port.
- The following five zones are set to 320 °C.
- The last two sections are set to 335 °C, to improve the filament surface quality and reduce instabilities at the extruder nozzle.

The diameter of the extruded filament is measured by a two-axis laser measurement system (from Zumbach). The target diameter is 1.75 mm, with a lower limit of 1.6 mm in order for the filament to be correctly pushed by the printing head gears, and an upper limit of 1.9 mm so that the filament can pass through the cylinder of the printing nozzle.

2.2. Susceptor filament characterization

After extrusion, the filament is characterized first by observing its cross-section using an Olympus GX-51 optical microscope. The porosity level is a critical parameter that must be controlled as it can lead to brittleness and inhomogeneous heating.

To analyze the magnetic properties of the filament, vibrating sample magnetometry (EV9 VSM from MircoSense) measurements are also performed on the extruded filament at 25 °C, 100 °C and 200 °C. Pure Ni particles are also analyzed with the same method at 25 °C to be compared with the filament.

The produced filament is then printed using an AON3D M2 printer equipped with a 0.4 mm nozzle. The nozzle temperature is fixed at 410 °C, the printing bed is fixed at 160 °C and the printing chamber at 135 °C. First, 1 mm-thick round samples (2 cm diameter) of printed susceptor are observed by optical microscopy to analyze the porosity level and the particle distribution after printing. For the sake of comparison, a similar 1 mm-thick 3D-printed film of CF/PEI is prepared using commercial filament from 3DxTech. Then, eight 0.6 mm-thick rectangles of PEI/Ni of 2 cm × 4 cm are printed and heated up by induction to measure their heating properties. Four samples of the same material produced by hot press compression moulding, as described in Ref. [7], are also characterized for comparison. The samples are placed on top of the induction heating coil and their temperature evolution is recorded using a FLIR A700 thermal camera. The measurement is performed on the side of the sample that is not facing the coil. Due to the small thickness of the samples, it is assumed that the temperature is uniform through the thickness. The detailed experimental procedure is

Table 1
Summary of the samples prepared for experimental characterization by VSM, optical microscopy and induction heating.

Experiment	Material	Quantity	Dimension/Mass
VSM	PEI/Ni-10%vol	3	Granules, 15 [mg]
	Ni	1	Powder, 41 [mg]
Optical microscopy	Printed PEI/Ni-10%vol	2	Discs, 20 [mm] of diameter, 1 [mm] of thickness
	Printed CF/PEI	2	
Induction heating	Printed PEI/Ni-10%vol	8	Rectangles, 40 [mm] by 20 [mm], 0.6 [mm] of thickness
	Pressed PEI/Ni-10%vol	4	

presented in Ref. [22]. The emissivity of the sample is fixed at 0.95. All the samples prepared for VSM, optical microscopy and induction heating are summarized in Table 1.

2.3. Susceptor deposition on honeycomb cores

PEI (ThermaX ULTEM 1010 filament from 3DxTech) honeycomb cores incorporating a layer of susceptor are produced using an AON3D M2 printer. The printed honeycomb cores are similar to those used in Ref. [7], with 4 mm wide hexagonal cells with 0.8 mm thick walls and a height of 10 mm. The bottom 1 mm-thick skin is also printed in PEI directly below the honeycomb cells, bringing the total thickness of the printed part to 11 mm. In this study, welding is therefore performed on one side only of the sandwich panel. The nozzle temperature is set to 390 °C, the bed temperature to 160 °C and the printing chamber temperature to 125 °C for the printing of PEI.

Then, layers of susceptor are directly printed on top of the PEI honeycomb core, using the secondary printing head of the AON3D M2 printer. In the slicer software Simplify3D, the printing procedure is set up to switch printing heads when reaching the final layers. It is important to properly calibrate both printing heads and their relative position. If this step is not conducted accurately, the secondary material deposition will be shifted compared to the previous layer, preventing good adhesion between layers.

The susceptor layer thickness is fixed at 1 mm, which is equivalent to five printed layers of 0.2 mm. This thickness is large compared to adhesives or other typical welding elements, this is to compensate for the fact that the printed susceptor does not cover the entirety of the surface, compared to a susceptor film, reducing its volume. Further, the susceptor will flow under pressure during the process, leading to a lower final thickness. The printing temperature of PEI is set to 390 °C, and susceptor printing to 410 °C. The difference in temperature is caused by the difference of viscosity of the two materials. Two susceptor deposition configurations are evaluated: a constant susceptor width, made of five 0.8 mm-wide layers on top of the cell walls (Fig. 2a), and an increasing susceptor width, varying from 0.8 to 2.4 mm in 0.4 mm increments. This corresponds to a width of two, three, four, five and six filaments in width per layer (Fig. 2b). The goal of increasing the width is to increase the amount of susceptor material at the interface, and therefore the heating rate. It also increases the contact surface area between the susceptor and the skin. For both configurations, a priming pillar is printed next to the honeycomb core. This part is composed of PEI layer and one single susceptor layer, which is printed before the actual honeycomb susceptor layer. As this is the first part printed after switching nozzles, it provides some time and space for the print to correctly initiate and ensures that the susceptor is properly printed when the nozzle moves to the honeycomb core.

2.4. Sandwich panels assembly by induction welding

The printed honeycomb incorporating the susceptor layer can be directly welded to its skin, without any additional material. GF/PEEK laminates are used as skins, with a co-consolidated PEI layer at the welding surface, following the Thermabond process [7]. This allows to weld the skins at the welding temperature of PEI (around 280–300 °C), without risking to deconsolidate the PEEK-based parent laminate ([23, 24]).

Then, sandwich samples are assembled using the vacuum assisted induction welding (Vac-IW) method [7]. The honeycomb core incorporating the printed susceptor layer and the GF/PEEK skin are placed inside a vacuum bag, which applies a constant and homogeneous pressure on the sample during the entire duration of the process. Then, the induction coil moves linearly relative to the sample, heating up the printed susceptor at the welding interface. In the present study, a water-cooled copper hairpin coil (two straight square-section tubes of 10 mm × 10 mm of outer dimensions, with a length of 200 mm) equipped with a Ferrotron 559H (Fluxtrol) magnetic field concentrator (MFC) is used, as in previous work from the authors ([4,7]). The coupling distance between the coil and the top of the skin facing it is fixed at 2 mm for all the samples. The amplitude of the alternating current in the induction coil is fixed at 600 A and its frequency at 388 kHz.

Three welding speeds (relative displacement speed between the induction coil and the sample) are evaluated: 0.1, 0.15 and 0.2 mm/s. Welded sandwich samples are first characterized by observing the weld line profile by optical microscopy, then the skin/core strength is evaluated using flatwise tensile (FWT) test, following the ASTM standard C297. Steel blocks are bonded on each side of the welded sandwich samples with an EA9696 adhesive from Loctite®. This allows the samples to be mounted in the testing jig, as presented in Refs. [4,7]. Samples are then tested on an MTS Alliance RF/200 machine, equipped with a 200 kN load cell. The test speed is fixed at 0.5 mm/min, as per the ASTM standard. One sample is welded at each speed for each susceptor configuration to be tested in FWT, plus one extra sample of each configuration welded at 0.15 mm/s for optical microscopy observations, for a total of eight welded sandwich samples.

3. Results

3.1. Susceptor filament characterization

The susceptor filaments produced with the Leistritz extruder exhibit a smooth surface finish. The porosity level and Ni distribution are

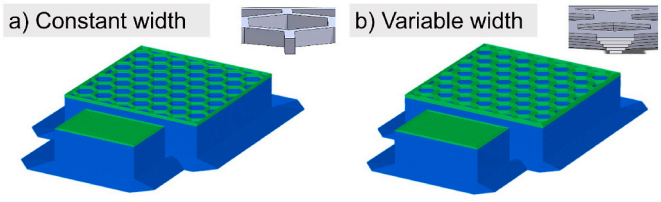

Fig. 2. Honeycomb core (in blue) including susceptor layer (in green) printing configurations: (a) constant susceptor width and (b) variable susceptor width. For both (a) and (b), an enclosed picture shows the detailed geometry of the susceptor layer. A priming pillar is produced prior to honeycomb printing.

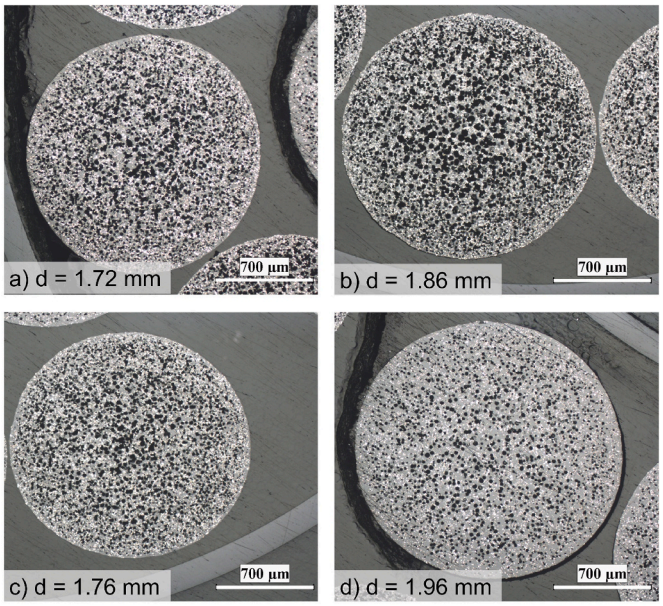

Fig. 3. Optical microscopy images of PEI/Ni-10%vol filament cross-sections. The white dots correspond to the Ni particles, and the black regions to voids. The mean diameter of each filament is reported on the corresponding figure.

analyzed by observing the cross-section of the filament by optical microscopy. Four representative filament pictures are presented in Fig. 3. The porosity level inside the filament varies significantly between samples, with a smaller quantity of visible porosities in Fig. 3d to a large amount in Fig. 3b. It also seems that porosities are larger towards the center of the filament. However, Ni particles appear to be well distributed in the PEI matrix, with no visible agglomerates.

The diameter of the filament is another important parameter that must be controlled during extrusion. As reported in Fig. 3, it varies around the target value of 1.75 mm. This is mostly caused by the absence of a mechanical pulling/winding system able to constantly pull the filament at the exit of the extruder. The filament should be pulled by a spooling system, however the extrusion was too slow for the available spooling device; thus, an operator was required to pull the filament by hand, while ensuring to stay in the desired diameter range by controlling the value on the diameter measurement device. To comply with the required 1.6–1.9 mm diameter range, sections of filaments that are out of this range were cut out. Remaining sections varied from 30 cm to more than 1 m, which is sufficient to print the different samples analyzed hereafter.

The filament's magnetic properties, measured using VSM, are presented in Fig. 4. First, the magnetic hysteresis of Ni particles and PEI/Ni-10%vol susceptor measured at 25 °C are compared. The maximum applied amplitudes are 16, 32 and 48 kA/m, yielding absorbed energy densities of 834, 2244 and 3504 J/m^3, respectively, for the Ni particles, and 445, 915 and 1351 J/m^3, respectively, for the PEI/Ni-10 % material. The selected applied amplitudes are in the range of the field amplitude of the AC magnetic field that is applied during the induction welding process [25]. In both Fig. 4a and b, the minor loops at the different amplitudes are clearly visible. As expected, the amount of hysteresis increases with increasing applied field amplitude. The saturation magnetization is not reached, even at 48 kA/m. The magnetization of the susceptor sample (Fig. 4b) is lower, because it is only composed of 10%vol of Ni particles, the rest of the sample – the PEI matrix – is not magnetic.

To better compare both materials, the hysteresis curves at 32 kA/m are presented in Fig. 5. The measured magnetic moment is normalized by the total mass of the sample in Fig. 5a (similar curves as in Fig. 4a and b), and by the mass of the Ni in Fig. 5b, assuming a volume fraction of 10 %. The curves overlap in Fig. 5b, which is a good indicator that the actual Ni concentration is 10%vol as expected. The shape of the hysteresis loop differs a little in the center, with a slightly lower coercivity for the susceptor, which can be caused by the difference of magnetic interactions between the particles. The enclosed surface areas of both hysteresis curves presented in Fig. 5b are calculated. Absorbed energy densities of 2244 J/m^3 and 2091 J/m^3 are obtained for the Ni particles and the PEI/Ni-10%vol susceptor, respectively, considering the volume of Ni particles.

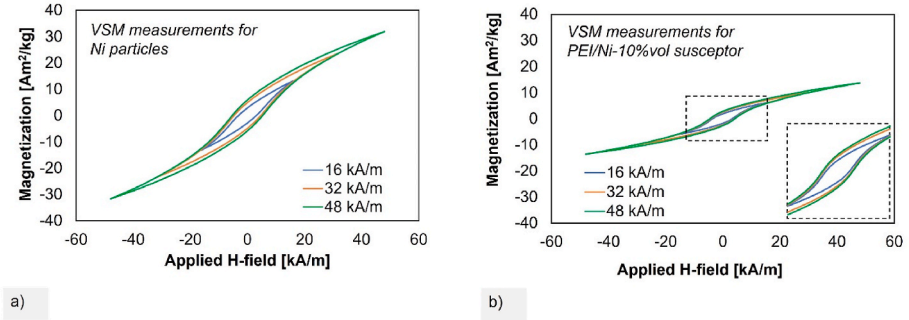

Fig. 4. Mass magnetization versus applied field for (a) Ni particles and (b) PEI/Ni-10%vol susceptor at 25 °C. Enclosed in (b) is a close-up view of the center of the magnetic hysteresis curves, as highlighted by the dashed black rectangle. The mass magnetization is obtained by dividing the measured magnetic moment by (a) the mass of Ni-particles, or (b) the mass of the sample.

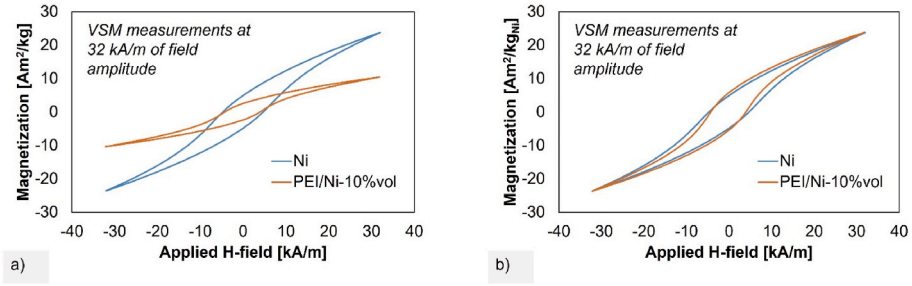

Fig. 5. Mass magnetization versus field for Ni particles and PEI/Ni-10%vol susceptor at 25 °C, with magnetization reported (a) per unit of mass of the sample and (b) per unit of mass of Ni, assuming 10%vol of particles in the susceptor.

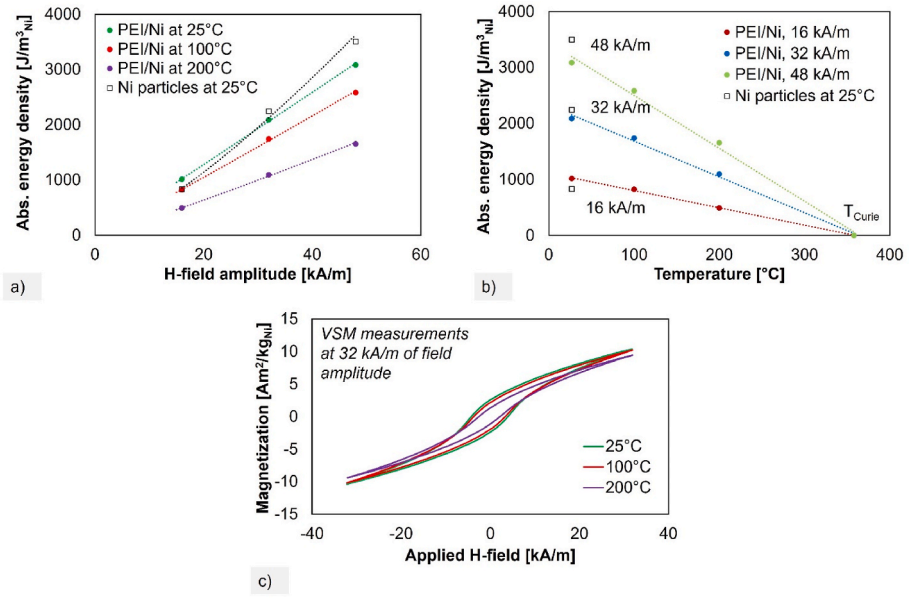

Fig. 6. Absorbed energy density of PEI/Ni-10%vol susceptor samples and Ni particles at different field amplitudes and temperatures, presented as a function of (a) the applied field amplitude, and (b) the temperature. Hysteresis curves of the PEI/Ni-10%vol susceptor samples tested at various temperatures under a field amplitude of 32 kA/m are presented in (c).

The evolution of the absorbed energy density of both Ni particles and susceptor is also measured as a function of temperature, to observe the expected decrease of magnetic properties. Measurements are conducted at 25 °C, 100 °C and 200 °C on the PEI/Ni-10%vol susceptor and at 25 °C on the Ni particles. The results are presented as a function of the maximum applied magnetic field in the hysteresis loop (Fig. 6a). The measurements follow the typical Steimetz equation [26].

The slope is somewhat different between the Ni particles and the PEI/Ni susceptor. This might be caused by the difference of magnetic interactions between Ni particles, as their packing fraction is different in the two samples. In the susceptor, the distance between particles is larger because of the PEI matrix. Ni particles alone are packed more densely, which can affect their magnetic response to the applied magnetic field during VSM measurements. In Fig. 6b, the same results are presented as a function of temperature, illustrating the decrease of the absorbed energy density with the increase of temperature. An extra data point at 358 °C is added corresponding to the Curie temperature of Ni at which the material has theoretically lost all magnetic ordering and show no magnetic hysteresis. The decrease is almost linear, which corresponds to what has been reported in the literature for Ni [27]. Finally, a comparison of the magnetic hysteresis of the PEI/Ni-10%vol susceptor tested at 25 °C, 100 °C and 200 °C under an applied field amplitude of 32 kA/m is presented in Fig. 6c. The decrease of the enclosed surface area, which corresponds to the absorbed energy density, is visible in this figure.

3.2. Printed susceptor characterization

Fig. 7 shows cross-section and in-plane views of a printed film of susceptor. The porosities that were observed in the filament are still present in the printed part. Overall, the dimensions of the printed part are comparable to the expected values, with a thickness close to 1 mm in Fig. 7a. There is good continuity between printed filaments, as their interface is not visible, in both cross-section and in-plane views, indicating a high degree of contact and welding between deposited layers. As observed in the filament before printing, the Ni distribution in the printed susceptor is homogeneous, with no signs of agglomeration, pointing to potential even heating during induction welding.

A cross section of the printed PEI/Ni-10%vol susceptor film is compared to a similar printed sample of commercial CF/PEI in Fig. 8. The apparent surface fraction of porosities is quantified by performing image analysis with the ImageJ software. Binary images extracted from Fig. 8a and b and used for the analysis are presented in Fig. 8c and d. For the PEI/Ni film, a surface concentration of 15.9 % of porosities is measured. It must be noted that the porosities with sizes close to the Ni particles diameter (approx. 5 μm) could be holes left by particles being pulled out during polishing and not actual porosities. As it is impossible to distinguish which fraction of the measured porosities are caused by this mechanism, it is not considered in the calculation. For the CF/PEI sample, a porosity level of 8.0 % is obtained. This is lower than in the printed susceptor, but large porosities appear in the same size range in

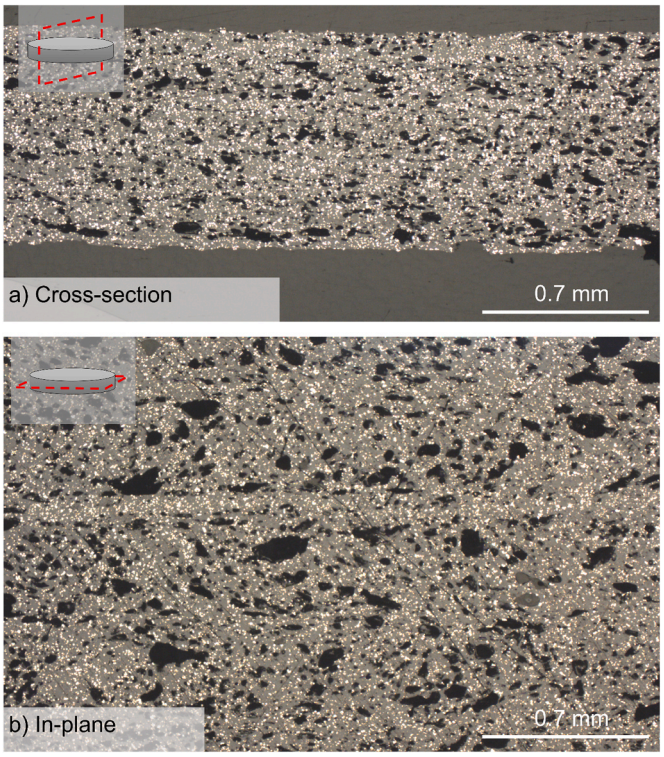

Fig. 7. Optical microscopy images of printed susceptor films (a) in cross-section view and (b) in in-plane view. The white dots correspond to the Ni particles. Enclosed schematics show the observed plane in the sample.

both materials. This is a good indicator that the quality of the susceptor filament is promising, although improvements can still be made to reduce the porosity level below 10 % and reach similar level as in commercially available composites filaments. In Fig. 8a and b, the concentration of filler is larger in the susceptor than in the commercial CF/PEI. This can also affect the porosity level and be responsible for the higher measured value. Reducing the Ni content, if the heating capability remains satisfying, could also help reducing the porosity level.

Finally, the induction heating capabilities of the printed susceptor are characterized. A total of eight printed samples are used. To put the heating properties of printed samples in perspective, four pressed samples of similar dimensions are produced, by forming the PEI/Ni-10%v material into films by compression moulding in a hot press at 320 °C ([7, 22]). These pressed samples are tested alongside the printed samples to ensure a proper comparison can be conducted (same coupling distance, room temperature, etc.)

Before characterizing their heating capabilities, the samples are first weighted, and their thickness is measured to evaluate their density (by simply dividing the weight by the sample volume). The average densities of the pressed and printed samples are 2.128 g/cm^3 (based on four samples, standard deviation of ±0.045 g/cm^3) and 1.443 g/cm^3 (based on eight samples, ±0.066 g/cm^3), respectively. The density of the printed samples is clearly lower than that of the pressed samples, likely due to the presence of the porosities previously described.

Following this preliminary characterization step, samples are heated up for 60 s, then the induction heating system is turned off; and the temperature is recorded for another 60 s. The temperature at the center point of the sample is extracted from the thermal camera data (Fig. 9). Due to the relatively small dimensions of the samples compared to the coil, the magnetic field, and consequently the heat generation, are assumed to be uniform in the sample, allowing the authors to report a single measurement at its center. The initial heating rate (slope of the

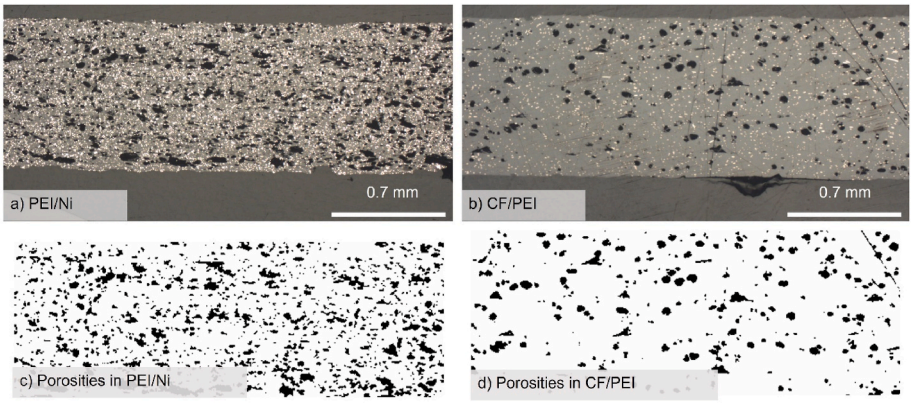

Fig. 8. Comparison of cross-section views of 3D-printed (a) PEI/Ni-10%vol susceptor and (b) commercial CF/PEI composite. Binary pictures used for image analysis representing the porosities in (c) PEI/Ni-10%vol printed susceptor and (d) commercial CF/PEI printed composite.

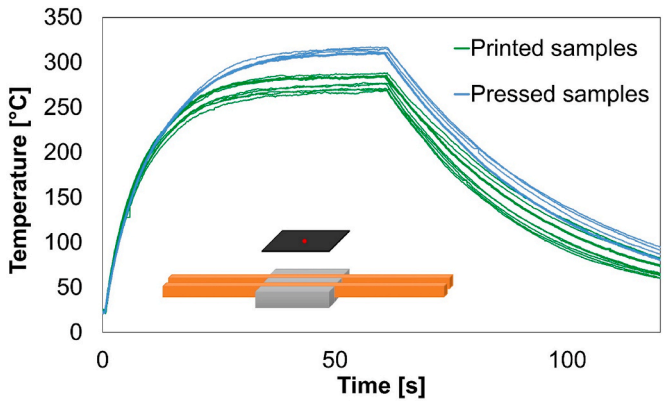

Fig. 9. Induction heating curves of pressed and printed susceptor samples. Enclosed is a scheme of the induction heating setup, with the red point indicating where the temperature evolution is recorded by the thermal camera.

curve at times close to 0) is very close for both pressed and printed susceptors. This indicates that they have a similar heating potential [22]. However, divergence is observed later during the heating. The printed susceptor samples reach lower temperature than the pressed ones, attributed to the lower density of the samples, caused by porosities. As fewer Ni particles are present in the same volume, less heat is generated. The printed samples also present a larger variability than the pressed samples. This needs to be addressed as it could lead to local differences in heating and in welding.

Fig. 10 presents the maximum temperature reached during induction heating tests as a function of the sample's density and the sample's weight, respectively. In Fig. 10a, the printed samples have a lower density, as discussed, causing the lower average temperature observed in Fig. 9. However, Fig. 10b shows that the variability of the measurements for both printed and pressed samples can be correlated to the mass of the sample, which varies according to the thickness of the samples. In the case of printed susceptor samples, this can be attributed to the variation of the filament's diameter. The slicing software, which prepares the instructions for the 3D-printer, assumes a constant diameter of 1.75 mm. However, if in reality the filament presents a different diameter, the printer cannot adjust and will extrude too much or too little material. Compared to a 1.75 mm filament, printing with a 1.6 mm filament represents a reduction of 16 % of the deposited material, or an increase of 18 % with a 1.9 mm filament. The tested printed samples exhibit thickness variability of the same range, indicating that the filament diameter variability is most probably responsible for the variations of thickness, which in turn impacts the heating variability.

3.3. Susceptor deposition on honeycomb cores

To verify the printability of the susceptor filament for a complex geometry, a susceptor layer is printed directly on top of a honeycomb core. One sample for each susceptor printing configuration is presented in Fig. 11; the pattern of the susceptor layer is correctly reproduced, and the deposition is clean and uniform across the surface of the sample. Close-up views of the printed susceptor layer indicate that there is no space between printed filaments inside the top layer.

Optical microscopy observation of the cross-section (Fig. 7) shows that porosities are still visible, especially towards the edges of the variable width layers (Fig. 12b), where no counter-pressure is present during printing, allowing the porosities to remain in their initial round shape. The overall shape of the deposited susceptor layer corresponds well to the expected printing geometry, as highlighted by the overlayed white dashed lines in Fig. 12c and d. This is an indication of the good printability of the susceptor and of the correct selection of the printing parameters. The visible excess of printed material (compared to the white dashed lines) indicates that the over-extrusion parameter, currently set at 1.1, could be slightly reduced.

Careful observation at the inter-filament interface reveals that no interface is visible. It also seems that the porosities are larger and more concentrated in the center of each filament, as previously noted in Fig. 3. This is beneficial for the inter-filament welding, as porosities in that area would prevent to reach complete degree of intimate contact. It can also be observed that the interface between pure PEI and PEI/Ni susceptor, presented in Fig. 12e is also very clean, without remaining separation line. This indicates that the printing parameters, especially the printing temperatures, are set correctly, allowing a good contact and a good welding between these two layers.

3.4. Induction welding of honeycomb cores with printed susceptor

Printed cores including a susceptor layer with the two presented geometries are welded to GF/PEEK skins. Welding speeds of 0.1, 0.15 and 0.2 mm/s are used. These welding speeds are lower than the speeds previously reported when using a susceptor film (0.5–0.9 mm/s [7]) as less susceptor material is present at the welding interface with a printed susceptor compared to a film susceptor. Also, as previously observed with the induction heating results, the printed susceptor has a slightly lower heating rate than the susceptor film.

The observations made on the 6 welded samples are summarized in Table 2. For the variable width susceptor layer, a good weld was obtained at a speed of 0.15 and 0.2 mm/s. At 0.1 mm/s, some core crushing is visible towards the back edge of the sample, indicating the presence of overheating in that zone. The location of the overheating zone towards the back edge can be explained: as the welding speed is very low, heat dissipated close to the front edge, at the beginning of the welding process, is conducted to the rest of the structure. Therefore, when the coil reaches the areas farther in the direction of the back edge, the sample is already hot, which changes the initial temperature and allows the susceptor to reach higher temperatures after application of induction heating, therefore inducing core crushing.

On the other hand, the constant width susceptor layer presents good welding at 0.1 and 0.15 mm/s. When welded at 0.2 mm/s, the sample

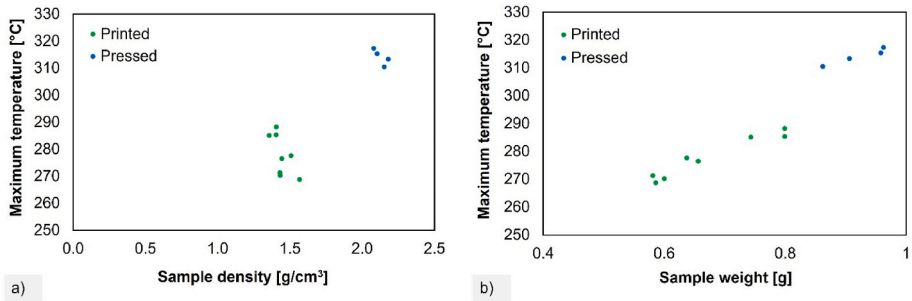

Fig. 10. Maximum temperature reached by pressed and printed susceptor samples during induction heating tests (a) as a function of the sample's density, and (b) as a function of the sample's weight.

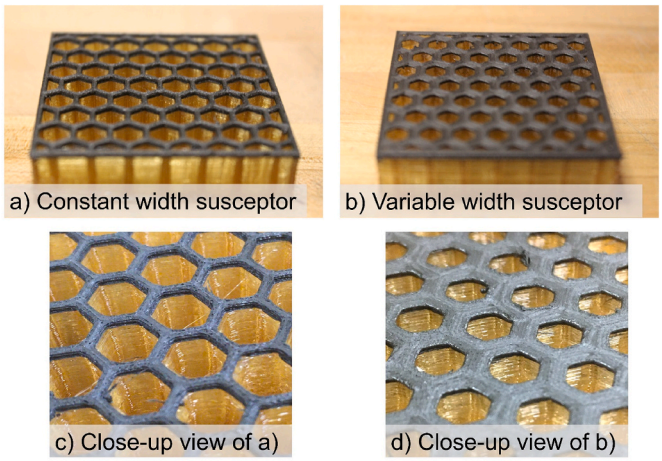

Fig. 11. Pictures of the susceptor layer printed on top of the honeycomb wall (a) with constant susceptor width and (b) with variable susceptor width. Close-up view of (a) and (b) in (c) and (d), respectively.

detached by itself when opening the vacuum bag after the process. In Table 2, the variable width susceptor layer presents a higher heating efficiency, allowing it to be welded faster. This is mostly caused by the larger volume of susceptor present at the weld line.

Welded samples are characterized by optical microscopy observations of the welded profile and FWT mechanical tests. Optical microscopy images of samples welded at 0.15 mm/s with both susceptor layer configurations are presented in Fig. 13. Deformation of the deposited susceptor layer and of the top of the cell walls is clearly visible. As expected from the observations in Table 2, more deformation occurred in the variable width susceptor layer (Fig. 13b), indicating that more heat was dissipated there. A consequence of that are the larger porosities visible in that sample. The porosities are fairly limited in the constant width susceptor, which also seems to be leaning towards one side of the cell walls. This is probably caused by a slight misalignment between the printed honeycomb and the printed susceptor. This is a good representation of the importance of properly calibrating the two printing heads.

Skin/core strength is evaluated by performing FWT tests on the welded sandwich panels (Fig. 14). The sample with a constant width of susceptor welded at 0.2 mm/s is not tested as it did not weld, but it is reported in the results as a zero strength to highlight that this speed is too slow. Samples welded at 0.15 and 0.1 mm/s exhibit a similar

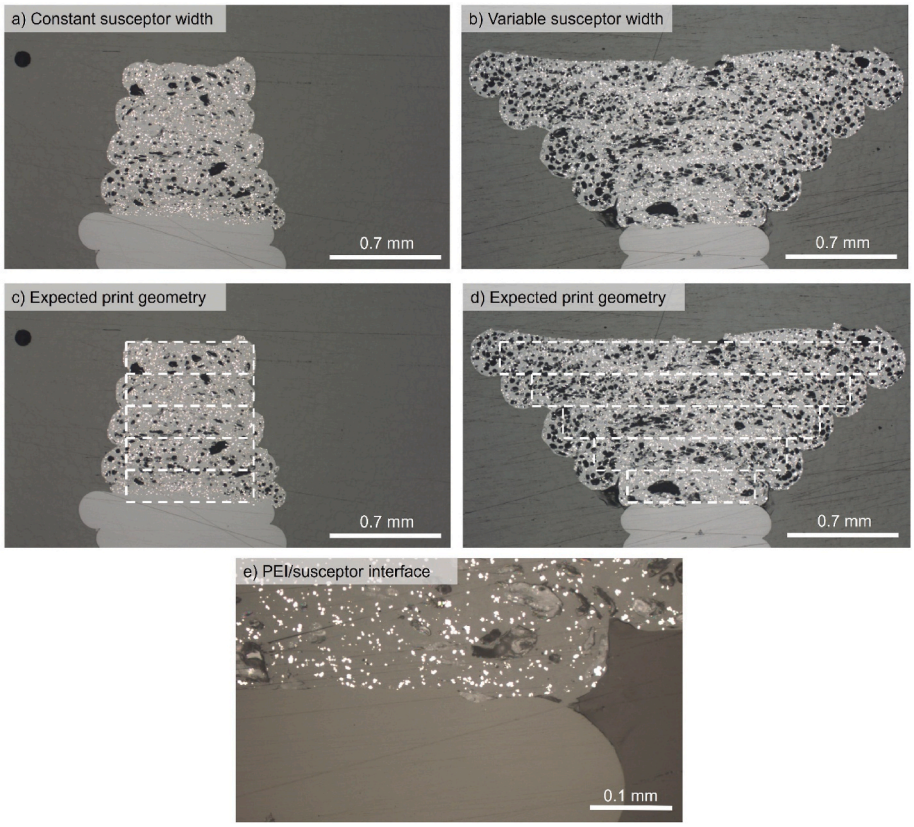

Fig. 12. Optical microscopy images of printed susceptor layer with (a) constant susceptor width and (b) variable susceptor width. Pictures in (c) and (d) overlay the expected print geometry in dashed white lines on the pictures (a) and (b). (e) is a close-up view of the interface between the PEI honeycomb and the PEI/Ni susceptor layer.

Table 2
– Summary of the welding of honeycomb cores incorporating a printed susceptor layer.

	Welding speed [mm/s]		
	0.1	0.15	0.2
Constant susceptor width	Good weld	Good weld	No weld
Variable susceptor width	Core crushing	Good weld	Good weld

strength (around 1.8 MPa). The failure mode in these two samples is cohesive in the susceptor layer (Fig. 15a and b), indicating that welding was achieved but the susceptor layer broke. This might be caused by the porosities inside that layer, and thus might be the maximum available strength with that material. Samples welded with a variable susceptor width exhibit higher strength. The sample welded at 0.2 mm/s reached 1.6 MPa, a strength similar to the samples welded at 0.1 and 0.15 mm/s with the constant susceptor width, despite the higher welding speed. This highlights the larger heating caused by the larger volume of susceptor present at the skin/core interface when using the variable susceptor width. That sample also exhibits a similar cohesive failure (Fig. 15e). Then, the sample welded at 0.15 mm/s broke at approximately 11.4 kN, which corresponds to a skin/core strength of 4.6 MPa. As visible in Fig. 15d, the failure mode is mostly core failure, indicating that the weld is stronger than the printed core, despite the presence of porosities. Finally, the sample welded at 0.1 mm/s could not be evaluated as failure occurred in the adhesive layer between the sample and the steel block.

These preliminary results provide valuable information. First, the printed susceptor layer requires a slower welding speed to reach sufficient welding, between 0.1 and 0.2 mm/s compared to 0.5–1.0 mm/s for susceptor films [7]. However, it is possible to obtain high strength and reach core failure with a printed susceptor. This is a major milestone to prove the feasibility of using printed induction welding susceptors to weld high-performance thermoplastics. The geometry of the susceptor layer has a large impact on the skin/core strength. The variable width provides a larger contact surface area between the skin and the core, which explains the increase in strength observed for the sample welded at 0.15 mm/s. Additionally, as more material is deposited in the variable susceptor width layer than in the constant width one, more heat is generated. As observed with the sample welded at 0.1 mm/s, too much heat was generated, which indicated that this geometry could be optimized (reduced overall layer thickness, Ni particles concentration, etc.). This could also further reduce the added mass of material, which

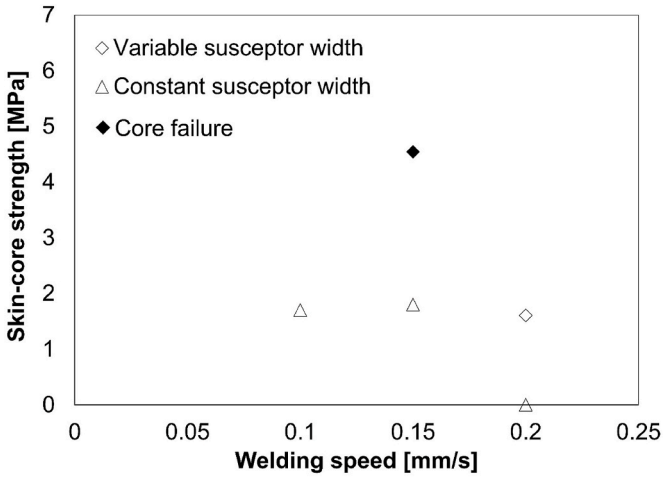

Fig. 14. Skin/core strength versus welding speed, obtained by FWT tests on sandwich samples welded with printed susceptor layer. The solid black diamond represents the sample that failed in the core.

represents currently 45 % of the mass of a susceptor film of equivalent thickness. The combination of larger contact surface area and larger heat generation explains the higher strength reached with the variable susceptor width. The welded skin/core strength is larger than the tensile strength of the core, where failure ultimately occurred.

When looking at the samples welded with a constant printed susceptor width, lower speed was required to reach welding. Once again, this is due to the minimal quantity of material that was added, leading to a lower amount of generated heat. However, this also means a smaller weight penalty due to the heating element (the printed susceptor with constant width represents only 26 % of the mass of a film of equivalent thickness), which can be favorable. It was still possible to reach almost 2 MPa of skin/core strength, which is a good result for a preliminary, proof-of-concept test. The cohesive failure observed for these samples indicated that the susceptor layer was partially welded, but it was mechanically weaker than the core. An improvement on the susceptor filament production leading to a reduction of the porosity level could be beneficial to increase the strength of the susceptor layer. Lower porosity levels would also increase the heating rate. Interestingly, the fact that the strength did not increase when reducing the welding speed from 0.15 to 0.1 mm/s gives several indications: first, it is not possible to

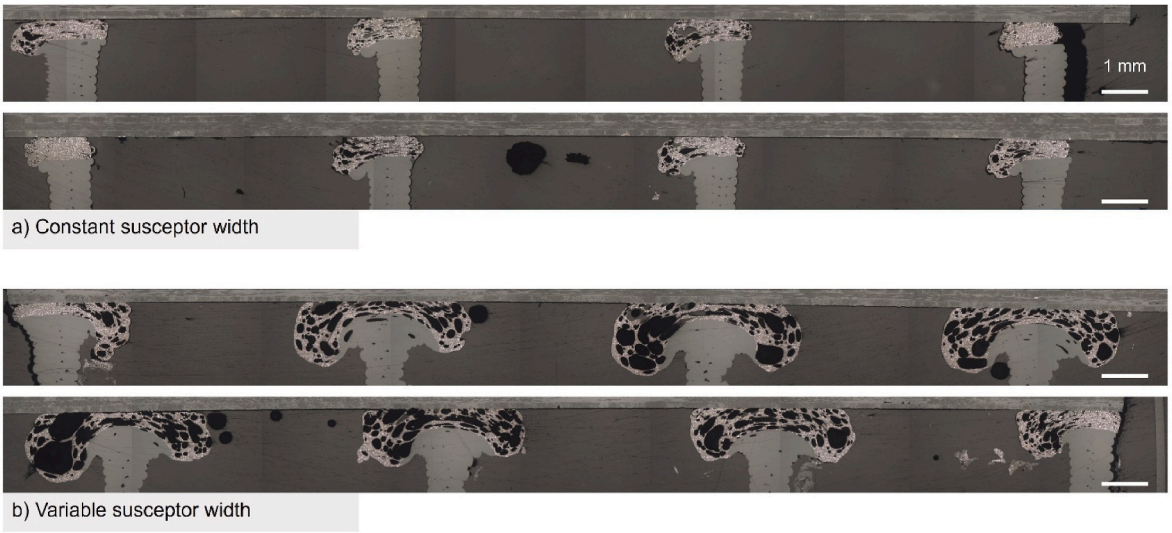

Fig. 13. Cross-section views of printed susceptor layers with (a) constant susceptor width and (b) variable susceptor width. The white scalebar represents 1 mm in each picture.

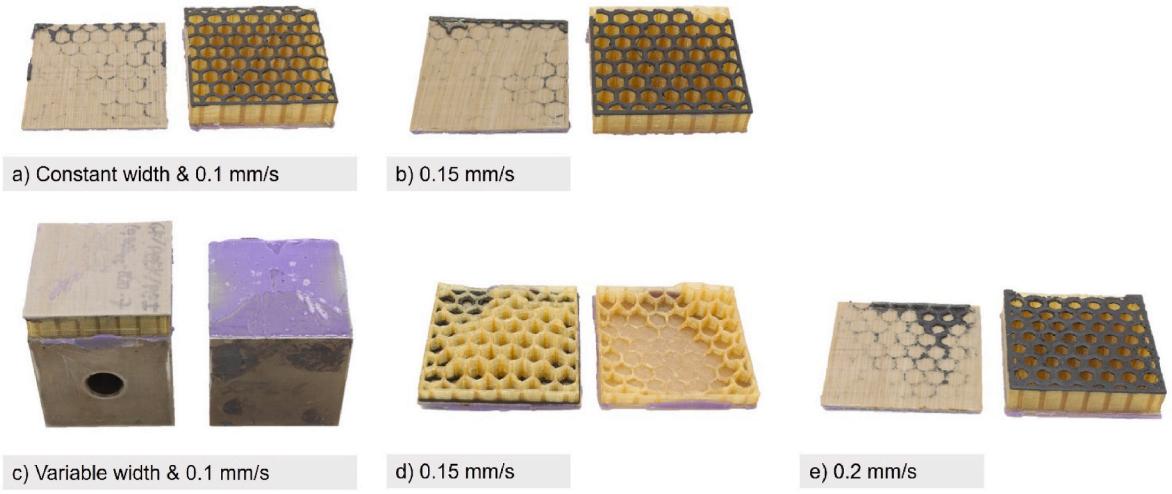

Fig. 15. Fractured FWT samples welded with (a) and (b) constant susceptor width and welding speed of 0.1 and 0.15 mm/s, respectively (no welding was obtained at 0.2 mm/s), and (c), (d) and (e) variable susceptor width welding speed of 0.1, 0.15 and 0.2 mm/s, respectively.

increase the degree of welding, meaning that 0.15 mm/s is a fast enough speed. Also, no overheating is observed, as no core crushing is visible, even at lower speed. That indicated that the susceptor cannot overheat in that configuration, once again highlighting the temperature-control feature of the hysteresis losses susceptors thanks to the Curie temperature of Ni. Finally, sources of improvements are not in the welding parameters but mostly in the materials development, by reducing the porosity level, selecting the optimal susceptor layer geometry and thickness, and its Ni content. The knockdown on the material's properties caused by the addition of particles and the presence of voids remains unclear. This should also be investigated to improve the welding process.

Another avenue to explore in the future is the pre-treatment of the Ni particles to improve their interfacial properties with the PEI matrix. This could compensate the loss of properties caused by adding particles in the polymer, as shown in past studies [28].

4. Conclusion

This paper presents a new method for joining sandwich structures by induction welding using a 3D-printed susceptor based on hysteresis losses. The discontinuous nature of the magnetic susceptor allows it to be manufactured in a filament shape and deposited on the honeycomb cores by additive manufacturing. The feasibility of producing and printing a susceptor filament for induction welding based on hysteresis losses is demonstrated. The PEI/Ni-10%vol susceptor produced in one single process step with an extruder showed promising heating results, although its properties could be improved by reducing the porosity level inside the filament and obtaining a more consistent filament diameter. Honeycomb cores incorporating printed susceptor layer were produced, showing the printability of the material on complex geometries. Finally, the weldability of the material was demonstrated by welding skins on the honeycomb cores and assessing their skin/core strength with FWT tests. The strongest sample resulted in a core failure at 4.6 MPa, indicating that the weld exhibits a higher strength than the core. These results, although preliminary, show the promising potential of printing hysteresis losses susceptors.

CRediT authorship contribution statement

R.G. Martin: Writing – original draft, Validation, Investigation, Formal analysis, Data curation. **C. Jonasson:** Formal analysis. **C. Johansson:** Writing – review & editing, Supervision, Formal analysis. **J. R. Tavares:** Writing – review & editing, Supervision, Resources, Funding acquisition. **M. Dubé:** Writing – review & editing, Supervision, Resources, Project administration, Methodology, Funding acquisition, Conceptualization.

Declaration of competing interest

The authors declare that they have no known competing financial interests or personal relationships that could have appeared to influence the work reported in this paper.

Acknowledgements

The authors acknowledge financial support from CREPEC (Research Center for High Performance Polymer and Composite Systems), NSERC (Natural Sciences and Engineering Research Council of Canada) (grant number ALLRP 556497-20), PRIMA Québec (Pôle de Recherche et d'Innovation en Matériaux Avancés) (grant number R20-13-004), the Canadian Space Agency (CSA), Ariane Group, NanoXplore inc, Mekanik and Dyze Design. They also want to thank Prof. David Ménard and Dr. Djamel Seddaoui (Polytechnique Montréal) for their help with the VSM measurements, as well as Mr. Arthur Lassus and Mr. Matthieu Gauthier (Polytechnique Montréal) for their help with the extrusion of the filament.

Data availability

Data will be made available on request.

References

[1] S. Yarlagadda, B.K. Fink, , et al.J.J.W. Gillespie, Resistive susceptor design for uniform heating during induction bonding of composites, J. Thermoplast. Compos. Mater. (2016), https://doi.org/10.1177/089270579801100403 août.
[2] R. Dermanaki Farahani, M. Janier, , et al.M. Dubé, Conductive films of silver nanoparticles as novel susceptors for induction welding of thermoplastic composites, Nanotechnology 29 (2018) janv, https://doi.org/10.1088/1361-6528/aaa93c.
[3] B.K. Fink, R.L. McCullough, , et al.J.W. Gillespie Jr., A local theory of heating in cross-ply carbon fiber thermoplastic composites by magnetic induction, Polym. Eng. Sci. 32 (5) (1992) 357–369, https://doi.org/10.1002/pen.760320509.
[4] R.G. Martin, C. Johansson, J.R. Tavares, , et al.M. Dubé, CF/PEEK skins assembly by induction welding for thermoplastic composite sandwich panels, Composites, Part B 284 (sept. 2024) 111676, https://doi.org/10.1016/j.compositesb.2024.111676.
[5] T. Bayerl, R. Schledjewski, , et al.P. Mitschang, Induction heating of thermoplastic materials by particulate heating promoters, Polym. Polym. Compos. 20 (2012) 333–342, https://doi.org/10.1177/096739111202000401, mai.

[6] W. Suwanwatana, S. Yarlagadda, , et al.J.W. Gillespie, Hysteresis heating-based induction bonding of thermoplastic composites, Compos. Sci. Technol. 66 (11) (2006) 1713–1723, https://doi.org/10.1016/j.compscitech.2005.11.009, sept.
[7] R.G. Martin, C. Johansson, J.R. Tavares, , et al.M. Dubé, Manufacturing of thermoplastic composite sandwich panels using induction welding under vacuum, Compos. Appl. Sci. Manuf. 182 (2024) 108211, https://doi.org/10.1016/j.compositesa.2024.108211 juill.
[8] R.G. Martin, C. Johansson, J.R. Tavares, , et al.M. Dubé, Material selection methodology for an induction welding magnetic susceptor based on hysteresis losses, Adv. Eng. Mater. 24 (3) (2022), https://doi.org/10.1002/adem.202100877.
[9] D. Bae, et al., Heating behavior of ferromagnetic Fe particle-embedded thermoplastic polyurethane adhesive film by induction heating, J. Ind. Eng. Chem. 30 (2015) 92–97, https://doi.org/10.1016/j.jiec.2015.05.007, oct.
[10] Y. Arbaoui, et al., 3D printed ferromagnetic composites for microwave applications, J. Mater. Sci. 52 (2017), https://doi.org/10.1007/s10853-016-0737-3 mai.
[11] A. Makridis, N. Okkalidis, D. Trygoniaris, K. Kazeli, , et al.M. Angelakeris, Composite magnetic 3D-printing filament fabrication protocol opens new perspectives in magnetic hyperthermia, J. Phys. Appl. Phys. 56 (28) (avr. 2023) 285002, https://doi.org/10.1088/1361-6463/accd01.
[12] G. Ehrmann, T. Blachowicz, , et al.A. Ehrmann, Magnetic 3D-printed composites - production and applications, Polymers 14 (sept. 2022) 3895, https://doi.org/10.3390/polym14183895.
[13] E. Palmero, et al., Development of permanent magnet MnAlC/polymer composites and flexible filament for bonding and 3D-printing technologies, Sci. Technol. Adv. Mater. 19 (2018) 465–473, https://doi.org/10.1080/14686996.2018.1471321, mai.
[14] I. Galarreta-Rodriguez, et al., Magnetically activated 3D printable polylactic acid/polycaprolactone/magnetite composites for magnetic induction heating generation, Adv. Compos. Hybrid Mater. 6 (3) (2023) 102, https://doi.org/10.1007/s42114-023-00687-4, mai.
[15] L. Zarybnicka, M. Pagac, R. Ševčík, J. Pokorny, , et al.M. Marek, Effect of topology parameters on physical–mechanical properties of magnetic PLA 3D-printed structures, Magnetochemistry 9 (2023) 232, https://doi.org/10.3390/magnetochemistry9120232, déc.
[16] T. Hanemann, D. Syperek, , et al.D. Nötzel, 3D printing of ABS barium ferrite composites, Materials 13 (6) (2020) 1481, https://doi.org/10.3390/ma13061481, mars.
[17] C. Huber, et al., 3D print of polymer bonded rare-earth magnets, and 3D magnetic field scanning with an end-user 3D printer, Appl. Phys. Lett. 109 (16) (oct. 2016) 162401, https://doi.org/10.1063/1.4964856.
[18] K. Sonnleitner, et al., 3D printing of polymer-bonded anisotropic magnets in an external magnetic field and by a modified production process, Appl. Phys. Lett. 116 (9) (2020) 092403, https://doi.org/10.1063/1.5142692 mars.
[19] L. Pigliaru, et al., 3D printing of high performance polymer-bonded PEEK-NdFeB magnetic composite materials, Funct. Compos. Mater. 1 (1) (2020) 4, https://doi.org/10.1186/s42252-020-00006-w, mai.
[20] A. Mazeeva, D. Masaylo, N. Razumov, G. Konov, , et al.A. Popovich, 3D printing technologies for fabrication of magnetic materials based on metal–polymer composites: a review, Materials 16 (21) (janv. 2023), https://doi.org/10.3390/ma16216928, 21.
[21] J. Grünewald, P. Parlevliet, , et al.V. Altstädt, Definition of process parameters for manufacturing of thermoplastic composite sandwiches – Part A: modelling, J. Thermoplast. Compos. Mater. (sept. 2017), https://doi.org/10.1177/0892705717729013.
[22] R.G. Martin, M. Figueiredo, C. Johansson, J.R. Tavares, , et al.M. Dubé, Characterization of magnetic susceptor heating rate due to hysteresis losses in thermoplastic welding, SAMPE J. 59 (5) (sept. 2023) 19–27.
[23] A. Smiley, A. Halbritter, F. Cogswell, , et al.P.J. Meakin, Dual polymer bonding of thermoplastic composite structures, Polym. Eng. Sci. 31 (7) (1991) 526–532, https://doi.org/10.1002/PEN.760310709, mai.
[24] F.N. Cogswell, P.J. Meakin, A.J. Smiley, M.T. Harvey, , et al.C. Booth, Thermoplastic interlayer bonding of aromatic polymer composites, in: *Composites Manufacturing*, Reno, NV, USA, 1989, pp. 2315–2325, mai.
[25] R.G. Martin, M. Figueiredo, C. Johansson, J.R. Tavares, , et al.M. Dubé, Hysteresis losses magnetic susceptor heating rate characterization, in: SAMPE Conference Proceedings. Seattle, WA, April 17 -20, 2023. Society for the Advancement of Material and Process Engineering – North America, 2023, pp. 1112–1127. Seattle, WA.
[26] F.J.G. Landgraf, M. Emura, , et al.M.F. de Campos, On the Steinmetz hysteresis law, J. Magn. Magn Mater. 320 (20) (oct. 2008) e531, https://doi.org/10.1016/j.jmmm.2008.04.011, e534.
[27] E.P. Harrison, XX. On the variation with temperature of the magnetic permeability of nickel and iron, London, Edinburgh Dublin Phil. Mag. J. Sci. 8 (44) (1904) 179–205, https://doi.org/10.1080/14786440409463188, août.
[28] Z. Zhang, et al., 3D printing of cellulose nanofiber/polylactic acid composites via an efficient dispersion method, Compos. Commun. 43 (nov. 2023) 101173, https://doi.org/10.1016/j.coco.2023.101173.